

Crustal *P*- and *S*-velocity structure of the Serbomacedonian Massif (Northern Greece) obtained by non-linear inversion of traveltimes

C. B. Papazachos

Institute of Engineering Seismology and Earthquake Engineering, PO Box 53, GR-55102, Foinikas, Thessaloniki, Greece. E-mail: costas@itsak.gr

Accepted 1997 December 10. Received 1997 November 2; in original form 1996 June 1

SUMMARY

In the present study, the *P*- and *S*-velocity structure of the crust and uppermost mantle in the area of central Macedonia (northern Greece) is presented, as derived from the inversion of traveltimes of local events. An appropriate preconditioning of the final linearized system is used in order to reduce ray density effects on the results. The study focuses mainly on the structure of the broader area of the Serbomacedonian Massif. Interesting features and details of the crustal structure can be recognized in the final tomographic images. The crustal thickness shows strong variations. Under the Serbomacedonian and western Rhodope massifs the crust has a thickness that exceeds 30 km. On the other hand, the North Aegean Trough exhibits a fairly thin crust (≈ 25 – 27 km). Moreover, the Serbomacedonian Massif is bounded by two regions that trend parallel to the Axios river–Thermaikos gulf and the Strymon river–Orfanou gulf, respectively, which show significant crustal thinning (≈ 25 – 28 km). The observed match between the direction of this crustal thinning and the basins' axes indicates that they have been generated by the same extensional deformation episode.

Key words: crustal structure, seismic tomography, upper mantle.

INTRODUCTION

The Aegean region (Fig. 1) is the seismically most active section of the Africa–Eurasia collision zone. The main feature of the area is the subduction of the eastern Mediterranean lithosphere under the Aegean (Papazachos & Comninakis 1969; McKenzie 1970, 1978; Le Pichon & Angelier 1979), which has a well-defined Benioff zone (Papazachos & Comninakis 1969, 1971). On the other hand, very high shallow seismicity is observed with thrust faults along the outer (convex) arc and mainly normal faults in the back-arc area (Comninakis 1975; McKenzie 1978). The complex geodynamic evolution of the area (Dercourt *et al.* 1986, 1990) has resulted in a complicated tectonic setting, which is also reflected in the velocity structure. In particular, the Aegean area exhibits strong velocity contrasts throughout its lithosphere. Traveltimes studies from earthquakes (Papazachos *et al.* 1966; Panagiotopoulos & Papazachos 1985; Papazachos *et al.* 1995) and explosions (Makris 1972, 1976; Voulgaris 1991) as well as gravity studies (Makris 1973; Chailas *et al.* 1992; Papazachos 1994) have revealed strong crustal thickness variations. As a result of the extension which is spread throughout the whole back-arc area, this area exhibits a thin crust of the order of 25–30 km, which locally thins up to 20 km. On the other hand, under the Hellenic Alps–Hellenic Arc accretionary prism, which is part of the Alpine belt, the crustal thickness locally exceeds 40 km.

The area of central Macedonia (northern Greece) is part of the Aegean back-arc area (Fig. 1). The main geological formations of the area are the Serbomacedonian and Rhodope massifs (Mercier 1968; Kockel *et al.* 1971), which comprise a mountainous and structurally complex domain of mainly metamorphic rocks and igneous bodies. The Serbomacedonian Massif is bounded on its western side by the sediments of the Axios basin, which continues into the Thermaikos gulf. Until recently the basin was considered to consist mainly of Neogene–Quaternary deposits, with a maximum thickness of 6 km in its southern part (Lalechos & Savoyat 1979). New data show the existence of a thick layer of Palaeocene deposits, which results in a maximum thickness of 11 km for the sedimentary deposits, located approximately in the central part of the gulf (Roussos 1994). The two massifs are separated by the Strymon basin, which consists of continental sediments with a maximum thickness of the order of 3–4 km (Mountrakis 1985). To the south the Serbomacedonian Massif is bordered by the Orfanou gulf and the North Aegean Trough, where Palaeogene sediments (Roussos 1994) also underlie the thick Neogene–Quaternary formations (1–5 km, Lalechos & Savoyat 1979) but their thickness is still unknown.

The whole area exhibits very high seismicity (e.g. Scordilis 1985), although it is quite far from the southern Aegean subduction. This is noticeable for the North Aegean Trough and the central Serbomacedonian Massif, where mainly dextral strike-slip and normal faults with occasional dextral strike-slip

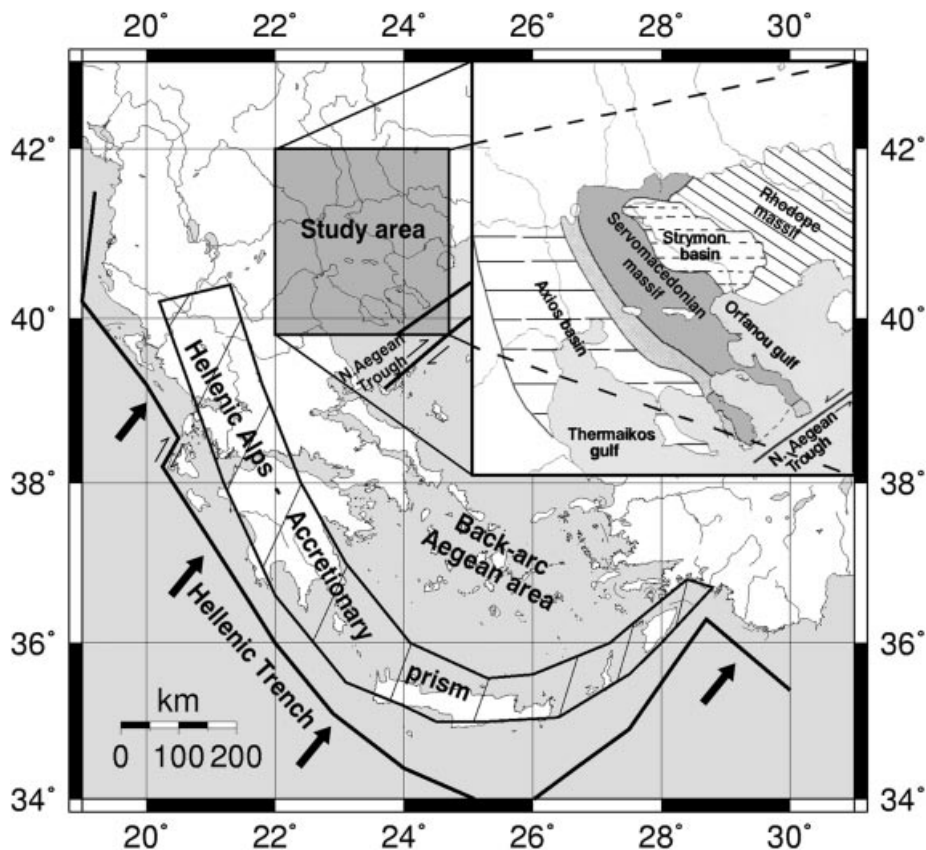


Figure 1. General features of the Aegean area. Details of the study area are shown in the inset.

components, respectively, are observed (e.g. Papazachos 1990). This mixed character is a result of the superposition of two different phenomena: NW–SE back-arc extension in the area and strike-slip deformation along the North Aegean Trough (Papazachos *et al.* 1993). This intensive deformation has resulted in the past in the formation of various local structures. A typical extensional structure is the Mygdonia graben, which is located in the centre of the Serbomacedonian Massif and is dominated by NW–SE (Miocene–Early Pliocene) and E–W (Quaternary) faults (Mercier *et al.* 1979; Psilovikos 1984; Mountrakis 1985; Papazachos *et al.* 1991). The relatively good coverage of the area by the seismological network of the Geophysical Laboratory of Thessaloniki has allowed the study of the velocity structure by the use of local (Scordilis 1985; Ligdas & Lees 1993) and teleseismic events (Christodoulou & Hatzfeld 1988).

In the present paper, the detailed characteristics of the velocity structure of central Macedonia (northern Greece) are studied. The main modifications from previous approaches are the use of a modified inversion technique which incorporates 3-D ray tracing, a larger amount of data and the inclusion of *S* waves, which have not been used previously. We mainly focus our attention on the Serbomacedonian Massif and its contacts with the Rhodope Massif, the North Aegean Trough and the Axios basin. For this reason a large data set ($\approx 41\,500$) of *P* and *S* traveltimes, from almost 3000 local events for the time period 1981–1992, was used. An appropriate preconditioning of the final linear system, using a crude estimate of the *a posteriori* covariance matrix, is applied in order to limit the artefacts in the tomographic images caused by irregular data

densities in our results. New information concerning the structure of the area can be recognized in the final results. The crustal thickness shows strong variations, with local crustal thickening up to 33–36 km beneath the two metamorphic belts (the Serbomacedonian and Rhodope massifs). On the other hand, the two basins that define the limits of the Serbomacedonian Massif exhibit a thinner crust (25–28 km), similar to the crustal thinning observed in the Northern Aegean (e.g. Brooks & Kiriakidis 1986; Papazachos *et al.* 1995), which is also confirmed in this study. Although the resolution is poorer for the *S* velocities, their general pattern correlates quite well with compressional velocities. Moreover, the shallow sedimentary basins show a much more significant signature in the *S* structure, due to the low *S* velocity of these formations.

TRAVELTIME DATA

The source of the data is the annual and monthly bulletins of the Geophysical Laboratory of the University of Thessaloniki (GLUT) for the time period 1981–1992. A small part of the data set came from the monthly bulletins of the seismological observatories of Greece and neighbouring countries. All events are relocated by GLUT using a local model for the area (Scordilis 1985). Moreover, we included data collected during a local experiment which was conducted in the area of Thessaloniki in 1986 (Hatzfeld *et al.* 1987). During this relocation procedure traveltimes were checked for outliers (phases with error larger than 2.5 s, phases with a $\sim \pm 60$ s error, etc.), which were removed from the final data set or appropriately corrected.

In the present study, only first arrivals are used, which are mostly P_g and S_g arrivals at short distances and P_n and S_n arrivals at larger distances. Since the data sources are quite inhomogeneous, the original phase identifications were not adopted and all late arrivals (e.g. suggested P_g waves at large distances) were discarded. Hence, after this removal, each phase was modelled as a first arrival. Unfortunately, no P_mP or S_mS arrivals that provide a good control for the crustal thickness are available in the bulletins. Although the lack of phase identification and reflected arrivals puts certain constraints on the data set, its resolving power is enhanced by the fact that most S arrivals are very accurate since almost all recording stations in the area have three-component sensors.

Since we did not want our results to be contaminated by mislocations, only data for events with at least nine P and S observations were used, in accordance with previous earthquake location studies (e.g. Scordilis 1985; Karakostas 1988). Also, since the data from different sources have a different accuracy, appropriate weights were used in the inversion for each traveltime data set. Therefore, based on the results of a previous study for the broader Aegean area (Papazachos *et al.*

1995), a higher weight (factor of ≈ 3) was assigned to all the arrivals of the local experiment (Hatzfeld *et al.* 1987) as the traveltime error for these data is approximately three times smaller than the corresponding error of recordings at regional stations. In a similar manner all regional arrivals were assigned a higher weight (factor of ≈ 2) if they were originally reported as impulsive arrivals. These weights were used throughout the whole inversion procedure and therefore affect both the final velocity model and the earthquake relocations. The final data set consists of $\approx 24\,500$ P and 17 000 S arrivals, recorded at 12 regional and 28 temporary stations. The final epicentres of the events for which data were used and the station locations are shown in Fig. 2.

INVERSION TECHNIQUE AND DATA PROCESSING

The principles of the inversion of traveltimes from local earthquakes are essentially those described in the original work of Aki & Lee (1976). The traveltime residual is a function of the perturbations of the event's hypocentral parameters and

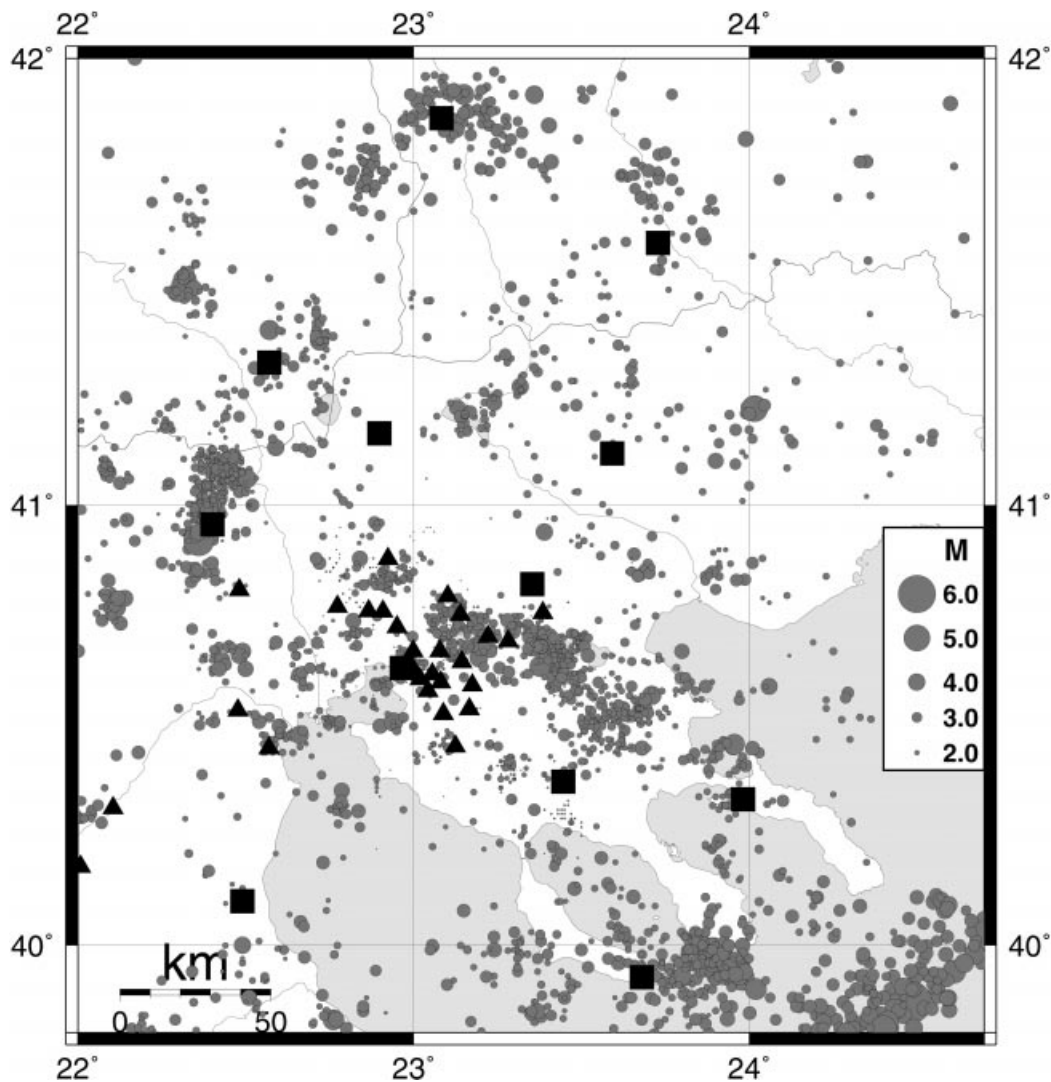


Figure 2. Map of the epicentres (denoted by circles) of the events for which data were used in the present study. Regional and temporary stations are shown as solid squares and triangles, respectively.

the velocity model. If this function is linearized using an initial approximate solution, a system of equations of the following form can be defined:

$$\mathbf{d} = \mathbf{A}\mathbf{x} = \mathbf{B}\mathbf{h} + \mathbf{C}\mathbf{v} + \mathbf{c}, \quad (1)$$

where \mathbf{d} contains the traveltime residuals, \mathbf{B} and \mathbf{C} are the hypocentral and velocity derivative matrices, \mathbf{h} and \mathbf{v} are the hypocentral and velocity correction vectors, and \mathbf{A} and \mathbf{x} simply combine matrices \mathbf{B} and \mathbf{C} and vectors \mathbf{h} , \mathbf{v} and \mathbf{c} . We also included a station correction vector, \mathbf{c} , in order to account for anything that cannot be explained by the velocity structure (e.g. local structure beneath a station, systematic time shifts at a station, etc.). Usually, a local representation is chosen for the velocity model such as a 3-D box car or a trilinear interpolation function (Aki & Lee 1976; Thurber 1983). Because of this choice the problem is treated as simultaneously overdetermined and underdetermined and cannot be solved in the usual least-squares sense by minimizing the data misfit. The standard technique is to construct an appropriate solution (Franklin 1970; Tarantola & Nercessian 1984; Constable *et al.* 1987) by considering additional constraints which lead to a solution with 'desirable' properties, for example minimization of the model or the model second derivative norm. In the present study, eq. (1) is modified (Papazachos & Nolet 1997a) as follows:

$$\mathbf{C}_d^{-1/2} \mathbf{A} \mathbf{C}_x^{1/2} \mathbf{S} \mathbf{H} \mathbf{z} = \mathbf{C}_d^{-1/2} \mathbf{d}, \quad \lambda \mathbf{I} \mathbf{z} = \mathbf{0}, \quad (2)$$

where \mathbf{C}_d is the data covariance matrix, \mathbf{C}_x is the *a priori* estimate of the model covariance matrix (usually diagonal), \mathbf{I} is the identity matrix, and \mathbf{S} is an appropriate smoothing matrix (e.g. Spakman & Nolet 1988). Therefore, a new linear system is formed which is solved in order to determine a new vector $\mathbf{z} = \mathbf{C}_x^{-1/2} \mathbf{S}^{-1} \mathbf{H}^{-1} \mathbf{x}$. Notice that for our final solution, \mathbf{x} , no additional matrix inversion is necessary as it is simply computed from \mathbf{z} using the relation $\mathbf{x} = \mathbf{C}_x^{-1/2} \mathbf{S} \mathbf{H} \mathbf{z}$. The smoothing matrix is a simple matrix which has a row sum of 1 and its effect is to 'redistribute' the elements of \mathbf{A} in its neighbourhood,

Table 1. Background 1-D velocity model for the Serbomacedonian Massif in the present study.

Depth (km)	V_P (km s ⁻¹)	V_S (km s ⁻¹)
-1	6.08	3.41
1	6.10	3.41
3	6.12	3.42
5	6.13	3.43
7	6.14	3.44
9	6.15	3.45
11	6.19	3.48
13	6.23	3.51
15	6.30	3.57
17	6.42	3.63
19	6.54	3.70
21	6.69	3.76
23	6.83	3.82
25	6.97	3.88
27	7.10	3.94
29	7.24	4.00
31	7.35	4.08
33	7.46	4.15
35	7.58	4.24
37	7.70	4.32
39	7.80	4.40

therefore introducing a spatial smoothing. Depending on the structure of \mathbf{S} this smoothing can be expanded or constrained, introducing a different extent of spatial smoothing which can vary both vertically and horizontally.

Here an additional diagonal scaling matrix of the form $\mathbf{H} = \text{diag}\{h_j^{-1/2}\}$ is included, where h_j is a measure of the j th column length of the matrix $\mathbf{A}' = \mathbf{C}_d^{-1/2} \mathbf{A} \mathbf{C}_x^{1/2} \mathbf{S}$. In this approach, $\mathbf{x}^T \mathbf{C}_x \mathbf{x}$ is minimized, instead of the usual $\mathbf{x}^T \mathbf{C}_x \mathbf{x}$, where $(\mathbf{C}_x^P)^{1/2} = \mathbf{C}_x^{1/2} \mathbf{S} \mathbf{H}$ is our preliminary estimate of the square root of the *a posteriori* model covariance matrix in an attempt to reduce relative errors in the final solution. \mathbf{C}_x^P is our educated guess for the *a posteriori* model covariance matrix; $\mathbf{C}_x^{1/2}$ contains the *a priori* error estimates which scale the various parameters

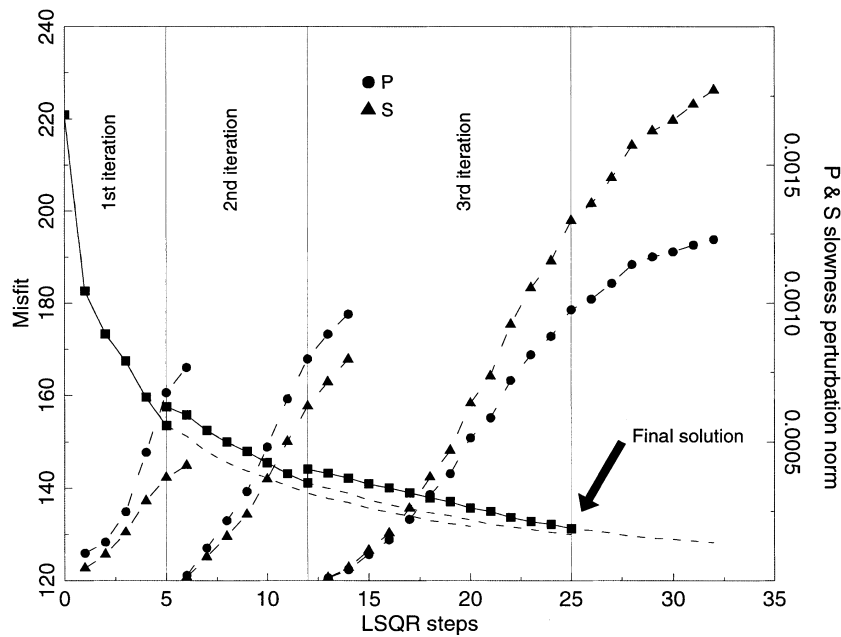


Figure 3. Plot of the misfit reduction (arbitrary units) and the model (P and S slowness perturbation) norm against LSQR steps.

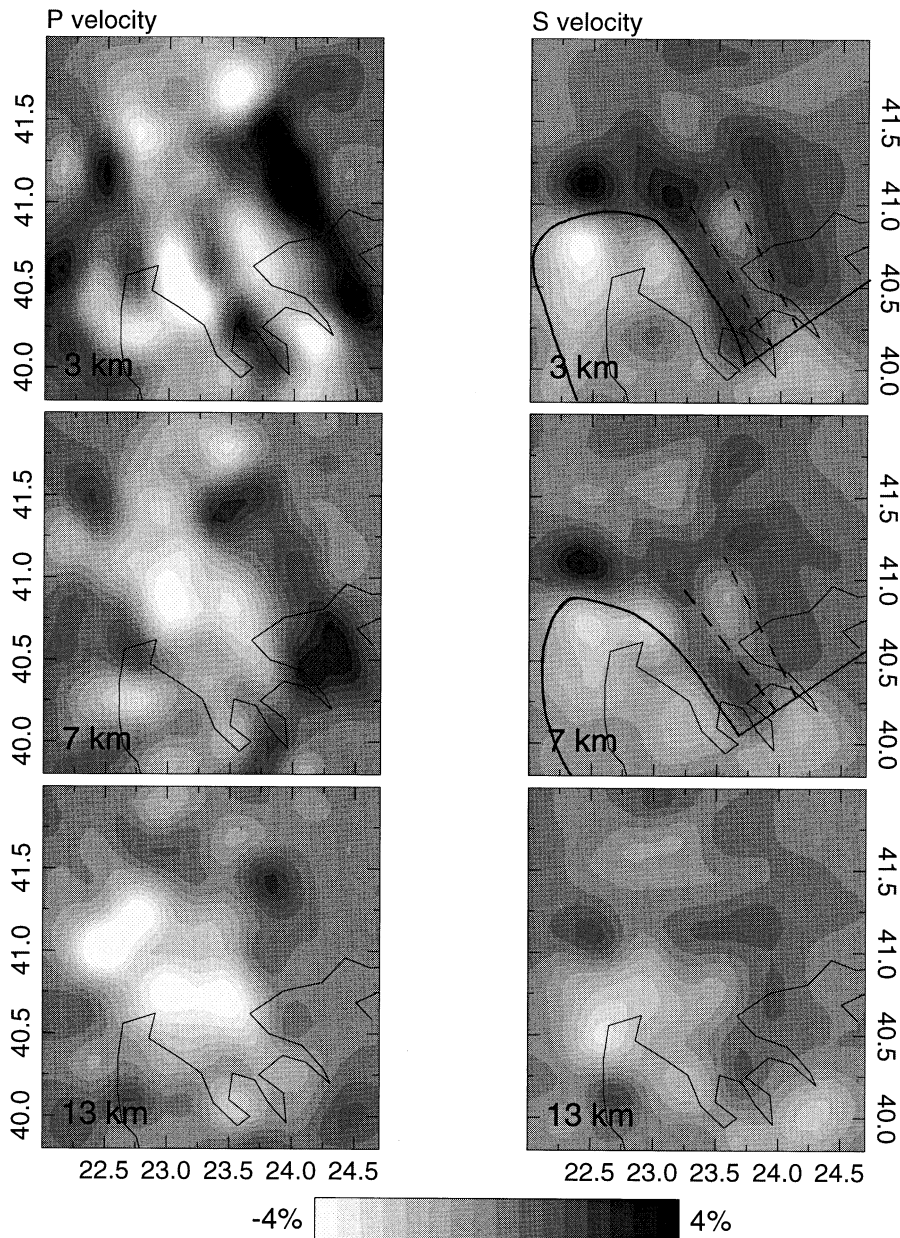


Figure 4. P - and S -velocity perturbations for the upper part (0–13 km) of the final 3-D model.

(velocities, hypocentral coordinates, station corrections), \mathbf{S} represents the correlation between neighbouring velocity nodes (smooth variations of the velocity field) and \mathbf{H} contains the observation that the *a posteriori* errors will vary inversely proportionally (e.g. VanDecar & Snieder 1994) to the square root of the ray length associated with each node (column norm of \mathbf{A}). For this reason, the incorporation of \mathbf{H} in the preconditioning of \mathbf{A} will minimize this effect (Papazachos & Nolet 1997a) and the inversion will not attempt to attribute higher anomalies in areas of high ray density (e.g. Sambridge 1990) since all *a posteriori* relative errors will be equalized. Therefore, an attempt is made to reduce significantly the effects of the ray distribution on the final tomographic results; that is, to anneal the correlation that is observed between areas of high ray density (large column length of matrix \mathbf{A}) and strong velocity perturbations

(Papazachos & Nolet 1997a). The constant λ regulates the additional minimum norm (damping) constraints.

For the model configuration, the earth is embedded in a rectangular grid of nodes and the slowness is defined for each node. The slowness at each point is calculated by trilinear interpolation. In our case, the grid consisted of 14 175 nodes for which both P and S velocities are defined. The horizontal and vertical grid spacings were set to 10 km and 2 km, respectively. Of course, for this model configuration a limited number of nodes lie outside the earth. However, the Cartesian geometry significantly speeds up all computations, therefore the small node redundancy is acceptable.

Initially, a 1-D background model was derived (Table 1), based on an initial model determined in a previous study (Papazachos *et al.* 1995). In order to eliminate the

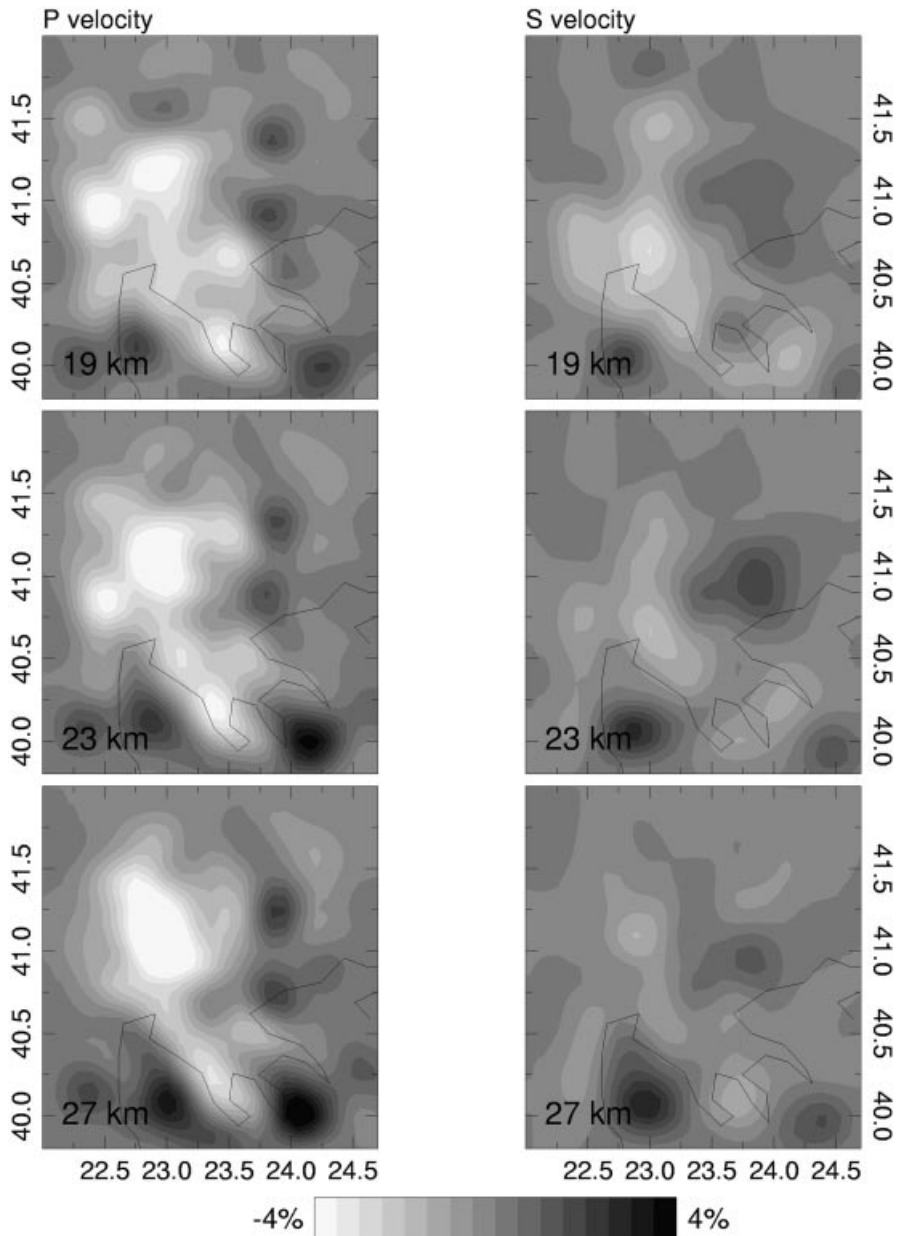


Figure 5. Same as Fig. 4 for the mid–lower-crustal part (19–27 km) of the final model.

effect of outliers, an exponential weight of the form $[1 + a \exp(b \cdot \text{residual})]$ was applied, which resulted in a fairly sharp cut-off for residuals larger than 2.5 s. These weights are included in the *a priori* covariance matrix of the arrival times. Based on previous estimates of the accuracy of hypocentral estimations (e.g. Scordilis 1985; Karakostas 1988), the values of 0.5 s, 0.5 s and 5 km for the standard errors of the station corrections, origin time and the hypocentral coordinates, respectively, were adopted after trials. For the slownesses, S_p and S_s , values of 0.02 and 0.035 s km^{-1} were accepted, respectively, based on previously published results for the area (Scordilis 1985; Ligdas & Lees 1993). Also, after tests, horizontal and vertical radii of 30 and 2 km, respectively, were defined for the smoothing matrix.

A large set of values between 0.1 and 10 was tried for the damping coefficients, λ ; however, the final tomographic figures

exhibited similar characteristics in all cases. For this reason, we decided to rely on our *a priori* error estimates which are included in the data covariance matrix, \mathbf{C}_d , and therefore the value of $\lambda = 1$ was finally adopted. This value is equal to the theoretically expected value (e.g. Franklin 1970), if our *a priori* estimates for the data and model covariance matrices are correct. Since the residual distribution is not completely Gaussian, a higher damping value may ensure the robustness of the solution to the relatively larger number of outliers in the real residual distribution. However, this was not observed in our case when larger values were used. \mathbf{A} and \mathbf{d} were computed for the initial (1-D) model and the linearized system (2) was solved with LSQR (Paige & Saunders 1982). After several steps there was a rapid change in the rate of misfit reduction and the model-norm increase. At this point LSQR was stopped and \mathbf{A} was recomputed using a revised 3-D bending

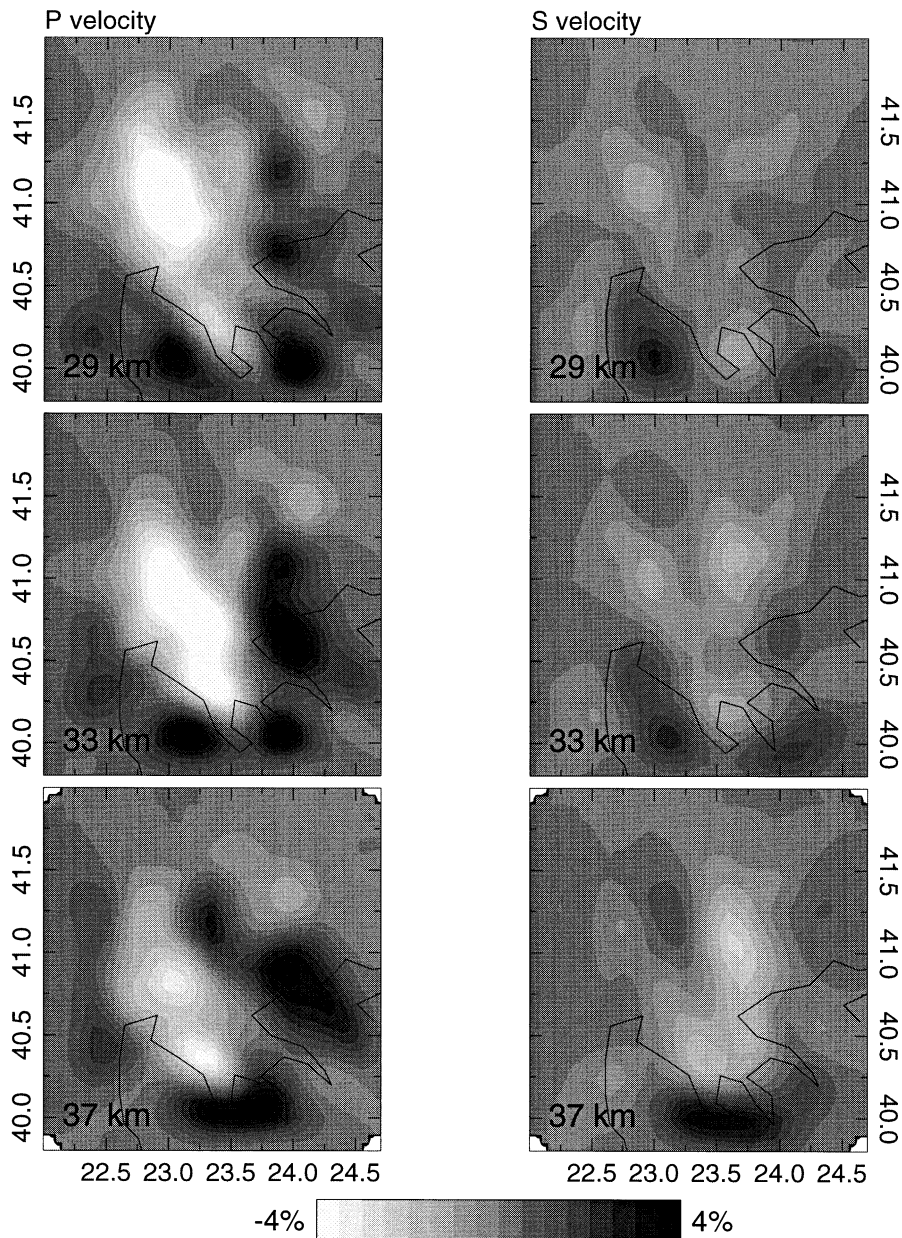


Figure 6. Same as Fig. 4 for the lower-crustal–upper-mantle part (29–37 km) of the final model.

ray-tracing algorithm (Moser *et al.* 1992). The efficiency of this algorithm when used in 3-D traveltimes tomography has been studied in detail by Papazachos & Nolet (1997b) and shows a significant improvement in the tomographic figures and, in particular, in the relative amplitude of the recovered velocity anomalies using a variety of synthetic tests.

After each iteration, the new linear system was solved again with LSQR and the whole procedure was repeated. Fig. 3 shows the variation of the misfit (arbitrary units) for each LSQR step. The P and S slowness norms are also plotted. These norms are defined as the norm of the slowness perturbation vector for each (P or S) velocity field. For every iteration these perturbations refer to the initial estimate derived by the previous iteration and not to the initial 1-D model before the inversion. Of course, these norms increase with LSQR steps as LSQR attempts to introduce larger velocity anomalies in

order to minimize the misfit. In our case we chose to stop after three iterations since no significant misfit improvement could be observed. Numerical tests indicate that, at least for the first iteration, LSQR should be stopped before convergence, since the observed misfit reduction is correct only for the linearized misfit estimate and might not be valid for a 3-D model because we deviate from the starting 1-D solution. This is also demonstrated in Fig. 3, where we observe a jump in the misfit between successive iterations. This occurs because between iterations we recompute \mathbf{A} and therefore estimate the true misfit, which is larger than the linearized estimate from the previous iteration, as also observed in other studies (Sambridge 1990; Papazachos & Nolet 1997b). The initial and final weighted combined (P and S) rms misfits for the inversion are 0.84 and 0.54 s, respectively.

Since the previous misfit reduction is a combined misfit,

because it includes P - and S -velocity perturbations as well as event relocations, it is difficult to estimate the contributions in this misfit of the various model parameters, especially of the P - and S -velocity model. In order to investigate this problem, we inverted matrix \mathbf{A} of the first iteration (calculated for the 1-D model) only for P -velocity perturbations and then only for S -velocity perturbations by setting all other perturbations to zero. For the P velocities the misfit reduction was equal to ≈ 60 per cent of the misfit reduction for the first iteration of the actual inversion performed in the paper where all parameters (P and S velocities, hypocentral parameters, station corrections) were included. This percentage drops to ≈ 30 per cent when only S velocities are determined. In order to compare these numbers they should be normalized with the corresponding number of P and S phases included in the inversion, since more P arrivals ($\approx 24\,500$) than S ($\approx 17\,000$) are used. However, even after this normalization the new P velocities improve the misfit by ≈ 40 per cent more than the S velocities. This result is expected if we consider that P arrivals are much more accurate than the corresponding S arrivals, even when three-component recordings are available, as in our case. Of course, such tests, as well as the resolution tests described later, have certain limitations since they are simple linear tests that can only be applied to a single matrix. Therefore, such tests cannot estimate the total contribution in the misfit reduction of different model parameters after more than one non-linear iteration and their results can only be used as a first approximation.

TOMOGRAPHIC RESULTS—RESOLUTION TESTS

Figs 4, 5 and 6 show the final P - and S -velocity distributions for different depths (≈ 4 km interval). As expected, both P and S velocities show a strongly varying pattern for all layers. The station corrections do not show any systematic pattern, therefore the velocity field is properly recovered. The P -velocity distribution is controlled mainly by the crustal thickness variations almost throughout the whole depth range (13–37 km), but most prominently for depths of 25–35 km. The Serbomacedonian Massif is delineated as a NW–SE-

trending zone of strong negative velocity perturbations. Since these are perturbations with respect to the background model, they indicate slow velocities within the belt and the existence of a thick crust under the belt. At the same time, the Serbomacedonian Massif is bounded by two similarly trending zones of positive velocity perturbations which correspond to the Axios and Strymon basins, respectively. These perturbations can be attributed to crustal thinning in the area. A second zone of positive anomalies (crustal thinning) is observed in the North Aegean Trough, in agreement with earlier tomographic (Papazachos *et al.* 1995), traveltime (Panagiotopoulos & Papazachos 1985) and gravity studies (Brooks & Kiriakidis 1986). It is interesting to note that all these zones of alternating positive and negative velocity anomalies trend almost NW–SE, which is in very good agreement with the well-known ‘Dinaric’ trend of the geological belts and the two basins of the area under study. In general, comparisons between Figs 5 and 6 (velocity variation for the middle–lower-crustal and upper-mantle layers) and Fig. 1 (local geology) show remarkable correlations.

The S velocities are fairly consistent with the corresponding P results. Although the resolution is relatively poorer for the deeper parts of the model, the S anomalies are very clear for the shallow layers. We observe low velocities for the sediments of the Axios basin–Thermaikos gulf and the North Aegean trough and a sharp velocity contrast with the metamorphic Serbomacedonian Massif. This limit is shown by a solid line for the first two S -velocity cross-sections. We also observe (Fig. 4) a possible signature (dashed line) of the Orfanou gulf–Strymon basin sediments. However, this anomaly is not so clear, possibly because the mean sediment thickness is at the limit of our resolving power in this area (2 km). The general pattern of the sedimentary formations is not so clear in the corresponding P images. This is probably due to the lower velocity contrast for the P waves, which are less affected than the S waves by the high water content in the formations of the sedimentary basins. For the deep layers there is a gradual transition of the S images to a similar pattern to that of the P results. However, the signature of the crustal variations is also observed for the S waves, especially around depths of 19–27 km. The lowermost part of the crust and the upper mantle

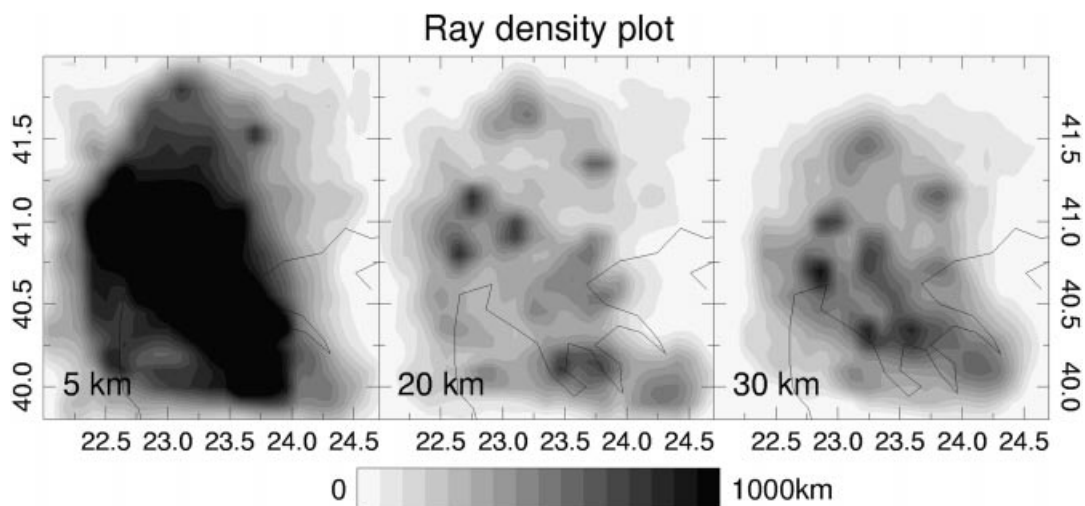


Figure 7. Ray density plots for three different depths of the area examined. The ray density for each velocity node is defined as the norm of the column of the derivative matrix \mathbf{A} , which corresponds to the ray length associated with this node. The grey scale varies linearly with the square root of this ray density.

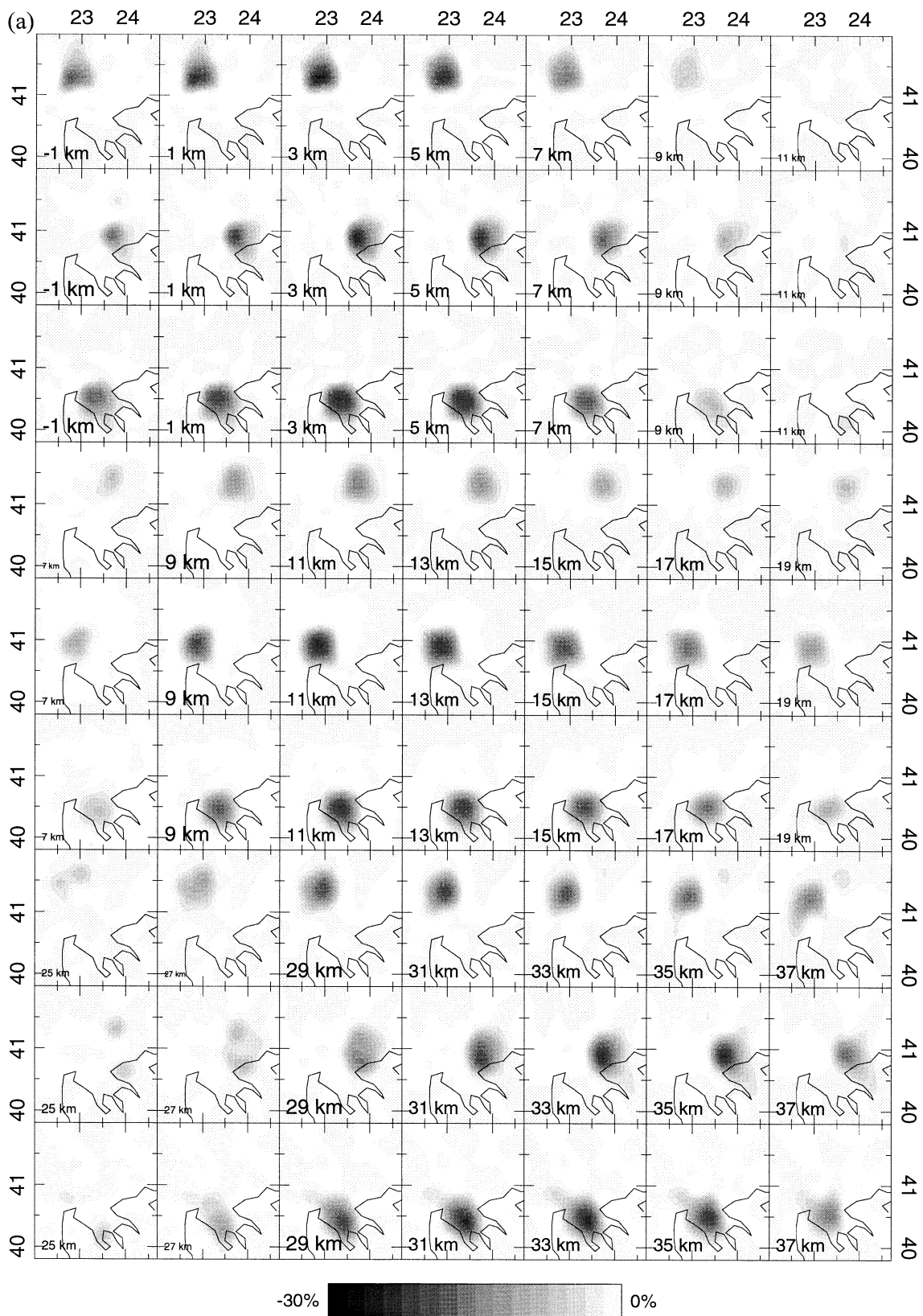


Figure 8. 3-D box-car resolution tests for (a) *P* and (b) *S* waves in three different depth ranges of the area examined. The first three rows in each figure correspond to three random velocity grid nodes in the uppermost crust (–1 to 7 km), rows 4–6 correspond to the middle crust (9–17 km) and the last three rows correspond to lower-crustal–upper-mantle layers (29–37 km). The input anomalies are square with a horizontal dimension of 40 km and extend throughout the depth ranges previously mentioned. Results are also shown for smaller and larger depths in order to assess the extent of vertical ‘leaking’ of the ‘energy’ of the input anomalies. The amplitude of the input anomalies is equal to the maximum of the scale bar shown in both figures. An adequate recovery of the shape and amplitude of the input anomalies is observed. The vertical ‘leaking’ ranges from ≈ 2 km in the central part of the model to 4 km for the middle crust and the borders of the model.

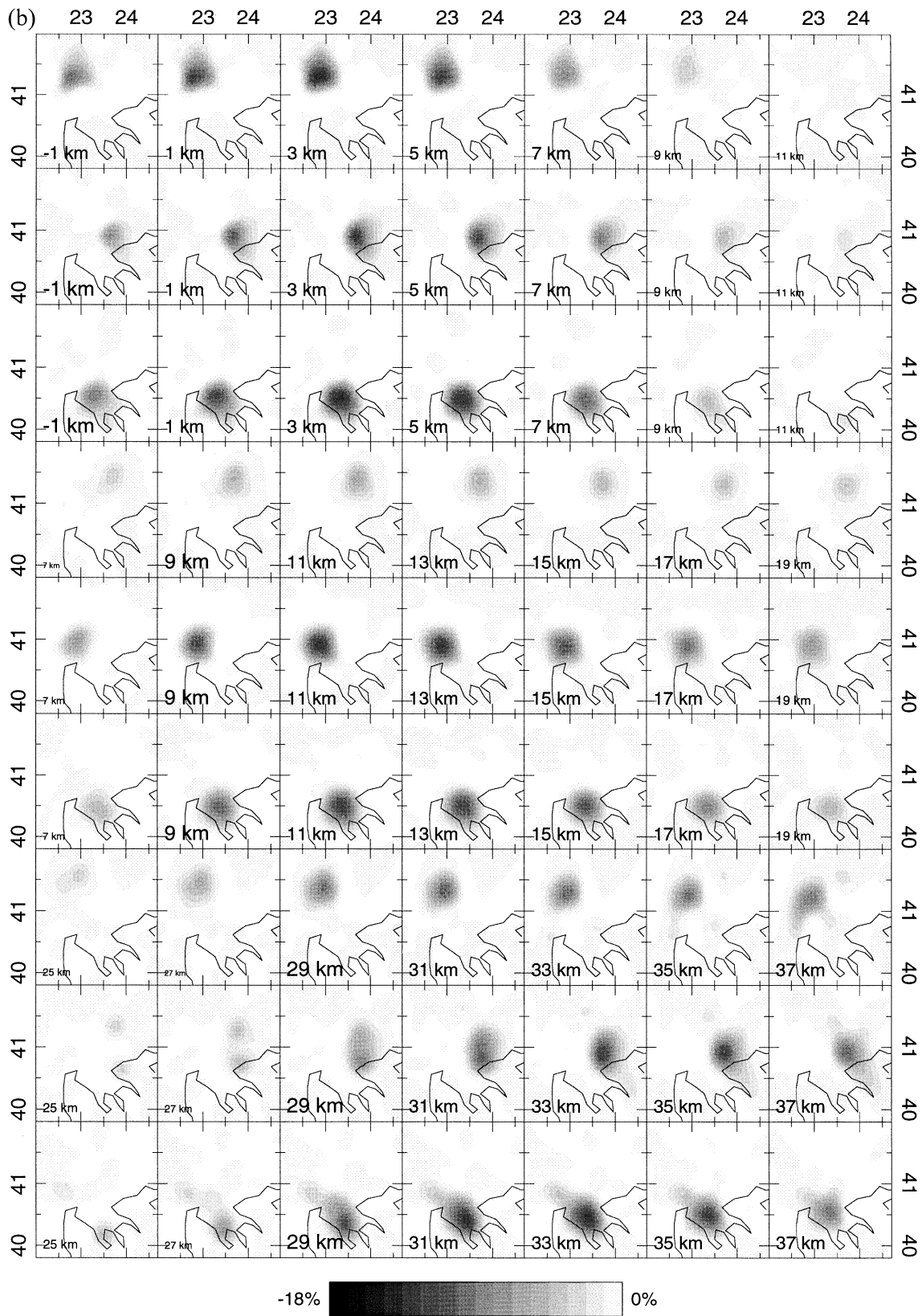


Figure 8. (Continued.)

are not visible to the deep crustal S^* and mantle S_n waves because very few of these arrivals are available in the data set due to their emergent waveforms being 'hidden' in the P coda, at least for the distance range that we have examined (less than ≈ 250 km).

Since eq. (1) was solved with LSQR we have no direct way of estimating the resolution and the errors involved in our calculations. Fig. 7 shows the ray density distribution for three different depths. Here the ray density is quantified by assigning to each velocity node the norm of the corresponding column of matrix \mathbf{A} , which corresponds to the ray length associated with this node. As errors depend on the square root of this ray length, an appropriate scale which varies linearly with this square root is used in this plot. We observe a fairly uniform distribution of the ray coverage, at least for the central part of the studied area.

In order to test the resolving power of our data we performed various cell-spike and box-car tests. Figs 8(a) and (b) show the results for some of these tests for P and S models, respectively. The input anomalies were square and extended to five node layers (vertical extent of 8 km). For both P and S , results are presented for three different depths, close to the top (surface to 7 km), middle (9–17 km) and bottom (29–37 km) of the model examined. For each depth, results for three randomly selected horizontal node positions are presented. The results for each of the different depths in each test are presented in Figs 8(a) and (b). For the layers where the original synthetic anomalies were put, the depth is indicated in a larger type. At shallower or deeper depths a smaller type is used to show the depth. The horizontal dimensions of the input anomaly were $\approx 0.4^\circ \times 0.4^\circ$ in all

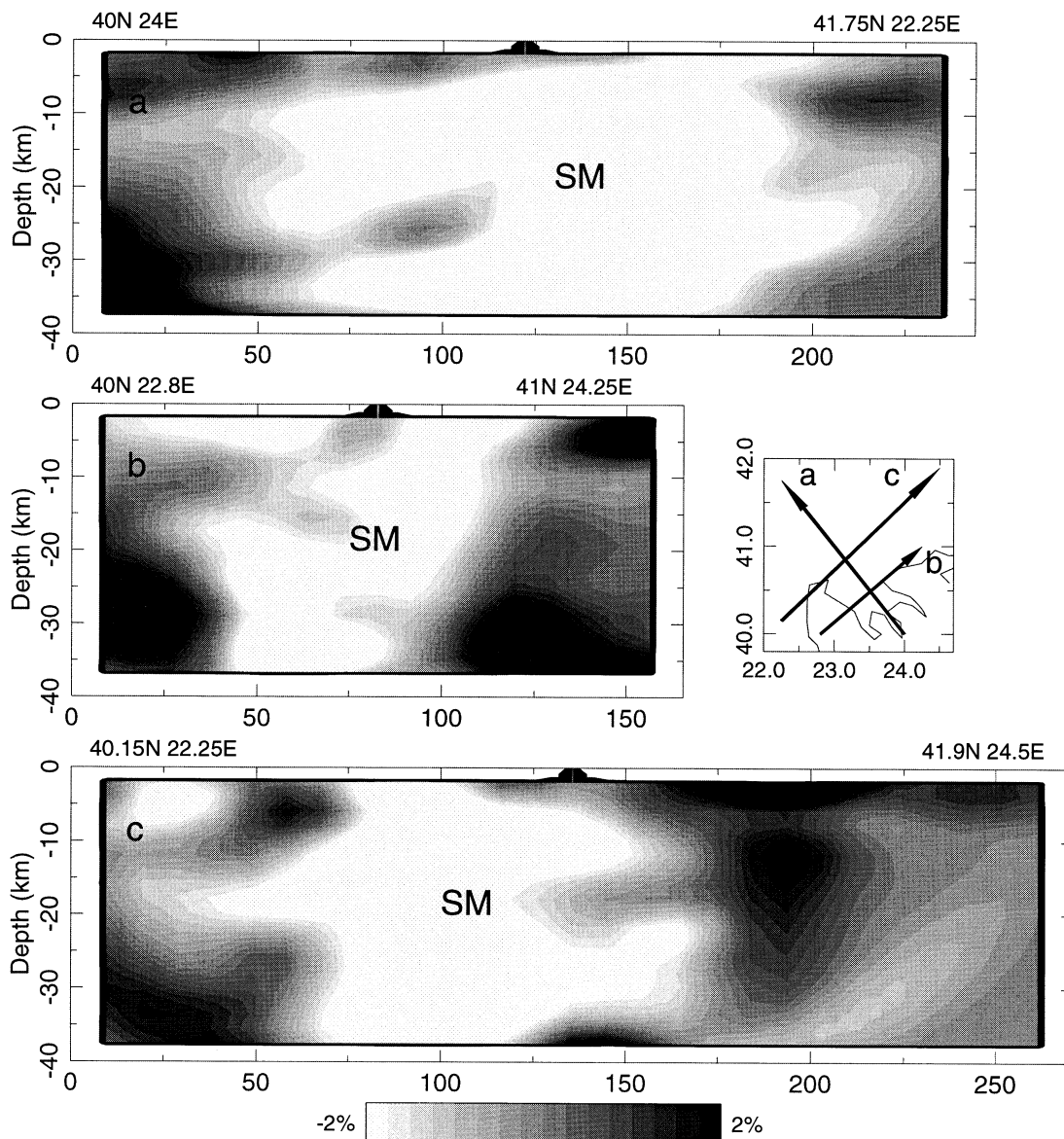


Figure 9. P -velocity perturbations presented for three cross-sections of the final velocity model. Notice in all figures the large body of negative velocity perturbations which corresponds to the Serbomacedonian Massif (SM). In (b) and (c) the Rhodope Massif can be observed in the eastern section of the profile.

cases, and the grey-scale maximum corresponds to the amplitude of the input synthetic anomaly. Since the input anomaly had the same slowness contrast for both *P* and *S* waves in all tests, the corresponding input velocity anomaly is larger for *P* waves.

For both *P* and *S* waves (Figs 8a and b) although the rectangular shape of the input anomalies was not recovered, the results show that the position of the input anomalies is retrieved well. Also, no serious artefacts are introduced in the recovered models. However, the relative amplitudes of the retrieved *P* and *S* anomalies are smaller than the input anomalies, with larger values for the nodes which lie in the middle layer of each five-layer input anomaly. Moreover, a vertical ‘leaking’ is observed both upwards and downwards from each input synthetic anomaly. The tests indicate that this ‘leaking’ is of the order of 2 km (in the central part of the

model) to 4 km (for the middle crust and close to the borders of the model). Therefore, the relative accuracy of the depth extent of any feature of the final tomographic results (Moho depths, etc.) should be considered to be of that order. On the other hand, such tests do not check the full resolving power of our inversion since they are only linear tests. For the real data, the additional non-linear iterations that have been performed will allow a much improved recovery of the true velocity anomalies, as already mentioned. Therefore, the previous estimates should be used as a lower limit for our resolving ability.

DISCUSSION

In Fig. 9 the *P*-velocity variations are plotted for three cross-sections. The first profile is parallel to the main axis of the

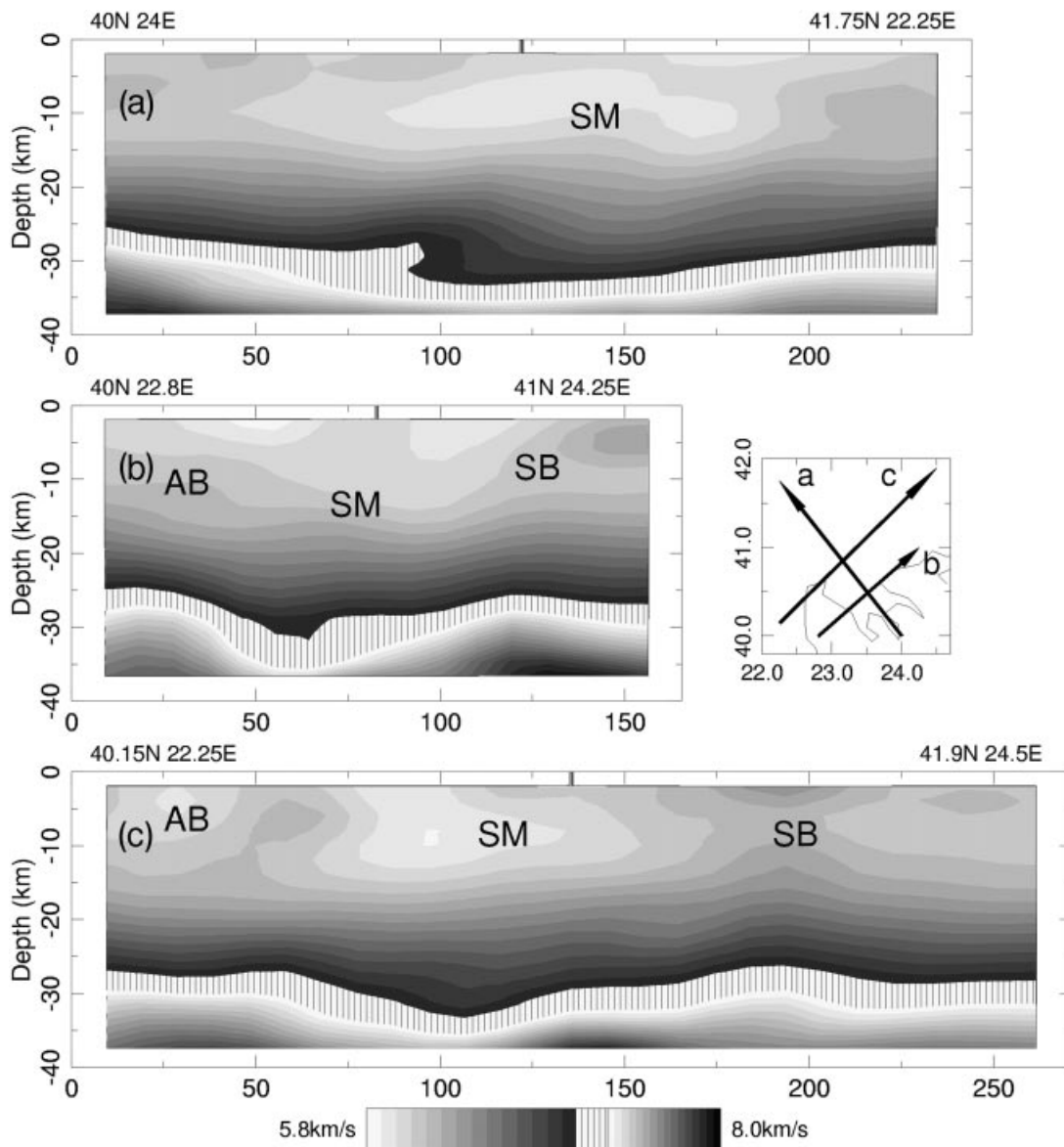


Figure 10. *P*-velocity distribution along the same cross-sections as in Fig. 9. The positions of the main geological formations (SM = Serbomacedonian Massif; AB = Axios basin; SB = Strymon basin) are shown on the profiles. The possible Moho limits are represented by the vertically hatched area, both in the cross-sections and in the grey-scale bar, and correspond to the velocity range between lower-crustal and upper-mantle velocities (see text).

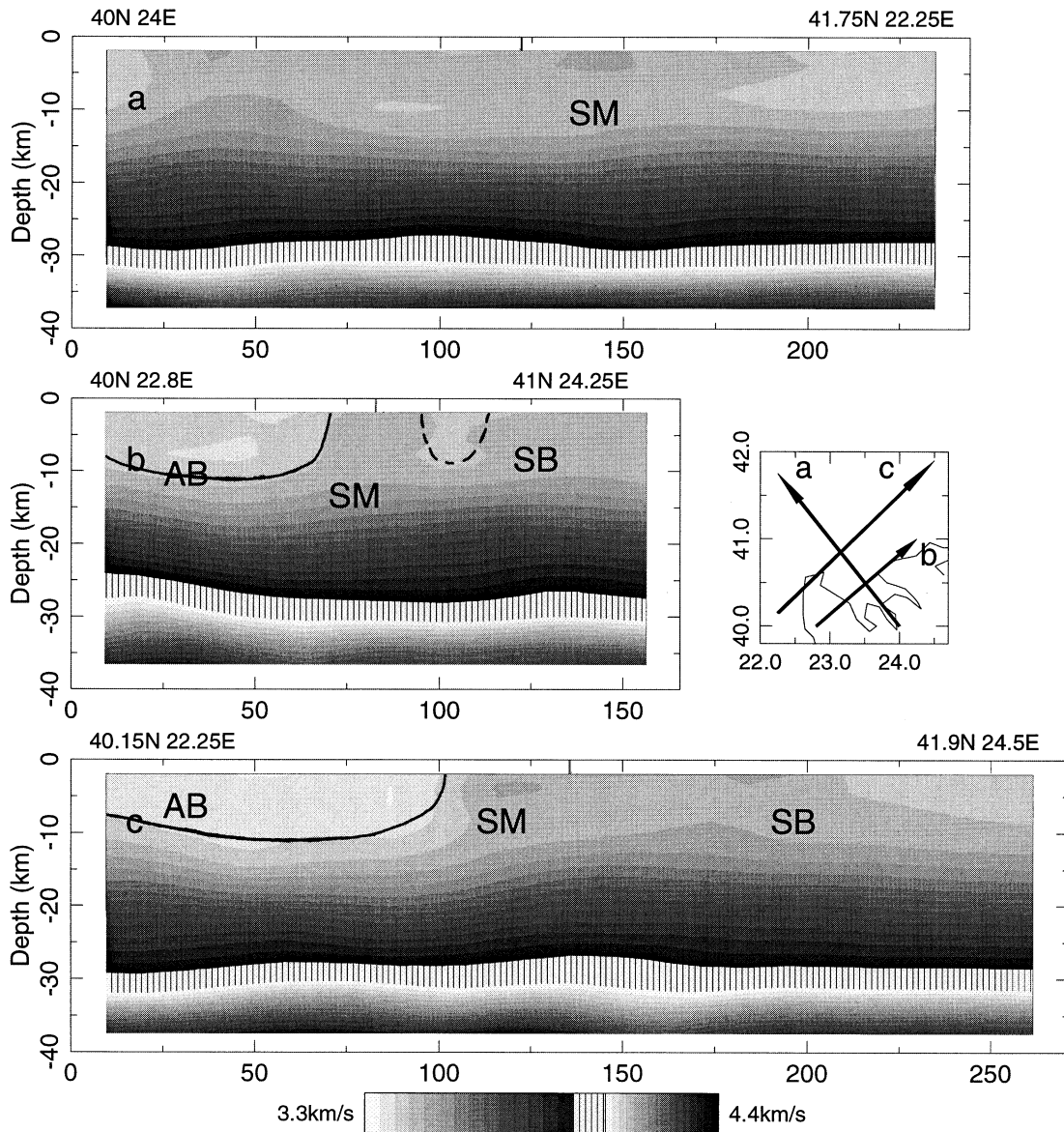


Figure 11. Same as Fig. 10 for the S -velocity field.

Serbomacedonian Massif (denoted as SM in the figures that follow). The massif is clearly recognized as a bulk of low velocity which is thickening in the centre of the belt and thinning towards its edges, especially towards the Northern Aegean Trough. The second and third profiles run almost perpendicular to the trend of the basins and the metamorphic belts. The Serbomacedonian Massif exhibits approximately the same characteristics, with a thick crust under its axis and two areas of crustal thinning, under the Axios and the Strymon basins (denoted AB and SB, respectively, in the figures that follow). On the northeastern border of both cross-sections, the western boundary of the Rhodope Massif has started to appear, exhibiting similar crustal thickening.

These crustal variations are clearly seen in Figs 10 and 11, where we have plotted the P - and S -velocity variations, respectively, for the same profiles. Because in the present study only P_g (S_g) and P_n (S_n) waves were used and the Moho is not directly modelled, it is difficult to infer accurate information about the crustal thickness. As an alternative, the velocity scale

for the P waves (Fig. 10) was separated into two ranges, 5.7–7.1 and 7.4–8.0 km s^{-1} . The mid-range (7.1–7.4 km s^{-1}) corresponds approximately to the average of the lower-crustal (6.6–6.8 km s^{-1}) and upper-crustal velocities (7.7–7.9 km s^{-1}) in the area (Makris 1976; Panagiotopoulos & Papazachos 1985). Therefore, this range approximately delineates the possible limits of the Moho discontinuity. The crustal thickness beneath the Serbomacedonian and Rhodope massifs reaches a depth of 34–36 km, whereas the basins exhibit crustal thicknesses of about 25–27 km. In the Northern Aegean Trough a thin crust (≈ 25 –27 km) is observed.

A similar approach was adopted for the S waves (Fig. 11). However, the crustal thickness variations are almost invisible in the lower crust and upper mantle due to the lack of rays penetrating these depths, as previously described. On the other hand, for the shallow layers we observe the low velocities of the sedimentary basins. Their limits are shown with solid lines. The maximum depth of sediments for the Axios basin (≈ 11 km) is in excellent agreement with the maximum depth

of the base of the Palaeogene sediments deduced from seismic reflection surveys and deep boreholes of the Greek Public Petroleum Company (Roussos 1994). In (b) we also observe an anomaly which is possibly due to the sediments of the Orfanou gulf, shown with a dashed line due to its shape and low amplitude.

The results are in good agreement with previous tomographic studies, although the velocity field obtained is much more 'enhanced', and *S* results are presented for the first time. Christodoulou & Hatzfeld (1988) used teleseismic arrivals to study the *P*-velocity structure down to ≈ 200 km. In their study the crust consists of a single layer (0–35 km) since the resolving power of their data was very crude. However, the results for this first layer indicate a thicker crust under the Serbomacedonian Massif. Ligdas & Lees (1993) performed a more detailed study using data from local events (≈ 6000 *P* phases). Their results also suggest the existence of low velocities for the shallow depths under the Axios and Strymon basins due to the sedimentary deposits. However, these authors did not compute a 1-D model but adopted a model from another area in the Aegean with a very high upper-mantle velocity (8.14 km s^{-1}). This very high P_n velocity in conjunction with the absence of *S* arrivals (which help to constrain earthquake locations) resulted in very distorted results for the deeper crust and uppermost mantle which do not allow the identification of the crustal thinning beneath the Axios and Strymon basins.

The crustal thinning under the Axios and Strymon basins is of special interest. The Axios basin is considered to have been created in the beginning of the upper Eocene. Up to the Oligocene the Axios basin was one of the largest areas of sedimentation in the Mediterranean, occupying a much larger area than today (Roussos 1994). However, both the Strymon and the Axios basins assumed their present NW–SE dominant elongation as a result of the Miocene–Pliocene NE–SW extensional field (Mountrakis 1985). For the Strymon basin recent results show that this extension started around the middle Miocene (Dinter *et al.* 1995). No accurate geochronological determinations exist for the Axios basin, where the extension that created the basin is generally considered to affect all post-Oligocene formations (Mountrakis *et al.* 1992). The results of this study suggest that this extension resulted in strong crustal thinning under the two areas that had the same NW–SE trend that is still observed today. Although the crustal thickness is only inferred from transmitted waves, we should not expect that the incorporation of additional data which are directly affected by the Moho (e.g. *PmP* reflections) would modify the main features of the crustal structure. On the contrary, the results presented in the present work are probably a smooth version of the true crustal thickness variations due to the damping which is incorporated in the inversion of the travel-time data (eq. 2). Therefore, the observed crustal thickness contrast of 7–11 km is probably a low limit of the true contrast. If we accept that this thinning is a result of a constant extensive deformation period which started in middle Miocene and lasted until the end of Pliocene (duration ≈ 14 Myr), we find a vertical strain rate, ϵ_z , of the order of $2\text{--}3 \times 10^{-8} \text{ yr}^{-1}$. This result is much smaller than recent estimates ($6\text{--}25 \times 10^{-8} \text{ yr}^{-1}$, Papazachos & Kiratzi 1996). A small part of this discrepancy might be due to the underestimation of the true crustal thinning. However, we may accept that the present deformation rates are representative of the area, even for a different, but

probably more important and widespread extensive deformation period such as that of the Miocene–Pliocene. In this case, this observed difference in deformation rates probably indicates that the extension did not occur uniformly in the time period but in much shorter time intervals, when deformation was more intense.

ACKNOWLEDGMENTS

The author would like to thank Prof. Papazachos for carefully reading the manuscript and for his fruitful suggestions. This research has been partly funded by the EEC project EV5 V-CT93–0281.

REFERENCES

- Aki, K. & Lee, W.H.K., 1976. Determination of three-dimensional velocity anomalies under a seismic array using first *P* arrival times from local earthquakes: 1. A homogeneous initial model, *J. geophys. Res.*, **81**, 4381–4399.
- Brooks, M. & Kiriakidis, L., 1986. Subsidence of the north Aegean trough: an alternative view, *J. geol. Soc. Lond.*, **143**, 23–27.
- Chailas, S. & Hipkin, R.G. & Lagios, E., 1992. Isostatic studies in the Hellenides, *Proc. 6th Congr. Geol. Soc. Greece*, Athens, **28(2)**, 587–599.
- Christodoulou, A. & Hatzfeld, D., 1988. Three-dimensional crustal and upper mantle structure beneath Chalkidiki (northern Greece), *Earth planet. Sci. Lett.*, **88**, 153–168.
- Comninakis, P.E., 1975. A contribution to the investigation of the seismicity of the area of Greece, *PhD thesis*, University of Athens.
- Constable, S.C. & Parker, R.L. & Constable, C., 1987. Occam's inversion: a practical algorithm for generating smooth models from electromagnetic sounding data, *Geophysics*, **52**, 289–300.
- Dercourt, J. *et al.*, 1990. Anisian to Oligocene paleogeography of the European margin of Tethys (Geneva to Baku), in *Evolution of the Northern Margin of Tethys: The Results of the IGCP Project 198*, eds Rakus, M., Dercourt, J. & Nairn, A.E.M., *Mem. Soc. Geol. Fr.*, **154**, 159–190.
- Dercourt, J. *et al.*, 1986. Geological evolution of the Tethys from the Atlantic to the Pamirs since the Lias, in *Evolution of the Tethys*, eds Auboin, J., Le Pichon, X. & Monin, A.S., *Tectonophysics*, **123**, 241–315.
- Dinter, D.A., Macfarlane, A., Hames, W., Isachsen, C., Bowring, S. & Royden, L., 1995. U–Pb and $^{40}\text{Ar}/^{39}\text{Ar}$ geochronology of the Symvolon granodiorite: implications for the thermal and the structural evolution of the Rhodope metamorphic core complex, north-eastern Greece, *Tectonics*, **14**, 886–908.
- Franklin, J.N., 1970. Well-posed stochastic extension of ill-posed linear problems, *J. Math. Anal. Appl.*, **31**, 682–716.
- Hatzfeld, D., Christodoulou, A.A., Scordilis, E.M., Panagiotopoulos, D. & Hatzidimitriou, P.M., 1987. A microearthquake study of the Mygdonian graben (northern Greece), *Earth planet. Sci. Lett.*, **81**, 379–396.
- Karakostas, B., 1988. Relation between the seismic activity and geological and geomorphological features of the Aegean and surrounding area, *PhD thesis*, University of Thessaloniki (in Greek).
- Kockel, F., Mollat, H. & Walther, H., 1971. Geologie des Servo-Macedonischen Massiv und seines mesozoischen Rahmen, *J. geophys. Res.*, **94**, 14 041–14 059.
- Lalechos, N. & Savoyat, E., 1979. La sedimentation Neogen dans le Fosse Nord Egeen, *VII Colloq. Geol. Aegean Region*, **II**, 591–603.
- Le Pichon, X. & Angelier, J., 1979. The Hellenic arc and trench system: a key to the neotectonic evolution of the eastern Mediterranean area, *Tectonophysics*, **60**, 1–42.
- Ligdas, C.N. & Lees, J.M., 1993. Seismic velocity constraints in the

- Thessaloniki and Chalkidiki areas (northern Greece) from a 3-D tomographic study, *Tectonophysics*, **228**, 97–121.
- Makris, J., 1972. Gravity and magnetic measurements on Peloponessus, Attica and Kithera and their preliminary interpretation, *Proc. XXIIIe Congr. Ass. Plen. de la CIESM*, Athens.
- Makris, J., 1973. Some geophysical aspects of the evolution of the Hellenides, *Bull. Geol. Soc. Greece*, **10**, 206–213.
- Makris, J., 1976. A dynamic model of the Hellenic arc deduced from geophysical data, *Tectonophysics*, **36**, 339–346.
- McKenzie, D.P., 1970. The plate tectonics of the Mediterranean region, *Nature*, **226**, 239–243.
- McKenzie, D.P., 1978. Active tectonics of the Alpine-Himalayan belt: the Aegean sea and surrounding regions, *Geophys. J. R. astr. Soc.*, **55**, 217–254.
- Mercier, J., 1968. Etude geologique des zone internes des Hellinides en Macedoine centrale, *Ann. Geol. Pays. Hell.*, **20**, 1–735.
- Mercier, J.L., Mouyaris, N., Simeakis, C., Rondoyannis, T. & Angelidhis, C., 1979. Intra-plate deformation: a quantitative study of the faults activated by the 1978 Thessaloniki earthquakes, *Nature*, **278**, 45–48.
- Moser, T.J., Nolet, G. & Snieder, G., 1992. Ray bending revisited, *Bull. seism. Soc. Am.*, **82**, 259–289.
- Mountrakis, D.M., 1985. *Geology of Greece*, University of Studio Press, Thessaloniki (in Greek).
- Mountrakis, D., Syridis, G., Polymenakos, L. & Pavlides, S., 1992. The neotectonic structure of the eastern boundary of the Axios-Thermaikos basin in the area of western Halkidiki (central Macedonia), *6th Congress Greek geol. Soc.*, Athens, **28(1)**, 379–395.
- Paige, C.C. & Saunders, M.A., 1982. LSQR: An algorithm for sparse linear equations and sparse least squares, *A.C.M. Trans. Math. Software.*, **8**, 43–71.
- Panagiotopoulos, D.G. & Papazachos, B.C., 1985. Travel times of Pn-waves in the Aegean and surrounding area, *Geophys. J. R. astr. Soc.*, **80**, 165–176.
- Papazachos, B.C., 1990. Seismicity of the Aegean and the surrounding area, *Tectonophysics*, **178**, 287–308.
- Papazachos, B.C. & Comninakis, P.E., 1969. Geophysical features of the Greek Islands Arc and Eastern Mediterranean Ridge, *Com. Ren. Seances Conf Reunie a Madrid*, **16**, 74–75.
- Papazachos, B.C. & Comninakis, P.E., 1971. Geophysical and tectonic features of the Aegean arc, *J. geophys. Res.*, **76**, 8517–8533.
- Papazachos, B.C., Comninakis, P. & Drakopoulos, J., 1966. Preliminary results of an investigation of crustal structure in southeastern Europe, *Bull. seism. Soc. Am.*, **56**, 1241–1268.
- Papazachos, B.C., Kiratzi, A. & Papadimitriou, E., 1991. Regional focal mechanisms for earthquakes in the Aegean area, *Pure appl. Geophys.*, **136**, 405–420.
- Papazachos, C.B., 1994. Structure of the crust and upper mantle in SE Europe by inversion of seismic and gravimetric data, *PhD thesis*, University of Thessaloniki (in Greek).
- Papazachos, C.B., Hatzidimitriou, P.M., Panagiotopoulos, D.G. & Tsokas, G.N., 1995. Tomography of the crust and upper mantle in southeast Europe, *J. geophys. Res.*, **100**, 12405–12422.
- Papazachos, C.B. & Kiratzi, A., 1996. A detailed study of the active crustal deformation in the Aegean and surrounding area, *Tectonophysics*, **253**, 129–154.
- Papazachos, C.B., Kiratzi, A.A. & Papazachos, B.C., 1993. Rates of active crustal deformation in the Aegean and the surrounding area, *J. Geodyn.*, **16**, 147–179.
- Papazachos, C.B. & Nolet, G., 1997a. P and S deep velocity structure of the Hellenic area obtained by robust non-linear inversion of arrival times, *J. geophys. Res.*, **102**, 8349–8367.
- Papazachos, C.B. & Nolet, G., 1997b. Non-linear arrival time tomography, *Ann. Geofis.*, **40**, 85–97.
- Psilovikos, A., 1984. Geomorphological and structural modification of the Serbomacedonian massif during the Neotectonic stage, *Tectonophysics*, **110**, 27–45.
- Roussos, T., 1994. Stratigraphy and paleogeographic evolution of the Paleocene molassic basins of the North Aegean area, *Bull. geol. Soc. Greece, Proc. 7th Cong Geol. Soc. Greece*, Athens, **30(2)**, 275–294.
- Sambridge, M.S., 1990. Non-linear arrival time inversion: constraining velocity anomalies by seeking smooth models in 3-D, *Geophys. J. Int.*, **101**, 157–168.
- Scordilis, E.M., 1985. Microseismic study of the Serbomacedonian zone and the surrounding area, PhD thesis, University of Thessaloniki (in Greek).
- Spakman, W. & Nolet, G., 1988. Imaging algorithms, accuracy and resolution in delay time tomography, in *Mathematical Geophysics*, pp. 155–187, eds Vlar, N.J., Nolet, G., Wortel, M.J.R. & Cloetingh, S.A.P.L., Reidel, Dordrecht.
- Tarantola, A. & Necessian, A., 1984. Three-dimensional inversion without blocks, *Geophys. J. R. astr. Soc.*, **79**, 299–306.
- Thurber, C.H., 1983. Earthquake locations and three-dimensional crustal structure in the Coyote Lake area, central California, *J. geophys. Res.*, **88**, 8226–8236.
- VanDecar, J.C. & Snieder, R., 1994. Obtaining smooth solutions to large, linear, inverse problems, *Geophysics*, **59**, 818–829.
- Voulgaris, N., 1991. Investigation of the crustal structure in Western Greece (Zakynthos–NW Peloponessus area), *PhD thesis*, University of Athens (in Greek).